Line shapes of ionizing Stark resonances in helium

A. Nussenzweig and E. E. Eyler*
Department of Physics, Yale University, New Haven, Connecticut 06511

T. Bergeman
Department of Physics, State University of New York at Stony Brook, Stony Brook, New York 11794

E. Pollack
Department of Physics, University of Connecticut, Storrs, Connecticut 06269
(Received 18 August 1989)

High-resolution laser spectroscopy is used to study the Stark effect in helium. The energies, widths, intensities, and shapes of resonances above the classical ionization threshold are measured for a wide range of electric field strengths. The high resolution of the lasers combined with careful design of the electric field plates allow accurate determination of the line-shape parameters, including linewidths and asymmetries accurate in the best cases to 6%. The WKB quantum-defect method is used to obtain detailed theoretical predictions for these Stark resonances with no adjustable parameters. Our study concentrates on the diabatic states of greatest slope arising from the zero-field $n=32$ and 40 manifolds in regions where these levels are fairly isolated and fit well to Fano profiles. In all cases, we obtain excellent agreement between experimental and theoretical line-shape parameters. A simpler autoionization model also reproduces the results, although less accurately.

I. INTRODUCTION

The Stark effect in Rydberg atoms has been extensively investigated both theoretically and experimentally since the pioneering work on alkali-metal spectra by Zimmerman *et al.*,[1] and measurements of field ionization in hydrogen by Koch and Mariani.[2] These investigations revealed, among other things, dramatic differences in the energy-level structure, ionization behavior, and line shape between hydrogenlike Rydberg atoms and hydrogen itself. In Rydberg atoms other than hydrogen, the core potential couples states with the same value of the azimuthal quantum number $|m|$, leading to numerous anticrossings. The character of the wave function changes rapidly in the regions of the avoided crossings, causing local anomalies in the ionization rates[3-6] and intensities.[7,8] In Na and He, otherwise stable states were observed to quench as they were coupled to nearby broader states.[4,6] The complementary line-narrowing effect, in which states become stable against ionization over a small range in field because of quantum interference, has also been observed, first in Rb by Feneuille *et al.*,[3] and then in Na by Liu *et al.*[5] Both groups measured the field dependence of the lifetimes of selected states near anticrossings. Photoionization measurements by the same groups also revealed that the line shapes for isolated states in the alkalis were distinctly asymmetric, in contrast to the Lorentzian line shapes predicted for hydrogen in the same field-energy region.[9,10] All of these manifestations of the non-Coulombic potential posed a challenge for theories that had accurately described the Stark structure in hydrogen.[11-13]

A major advance in the theory of the Stark effect in Rydberg atoms was made by Harmin,[14-17] who combined modified WKB approximations with quantum-defect methods in parabolic coordinates (WKB-QD) to predict the photoabsorption cross section in static electric fields using no adjustable parameters. Experimental line shapes with limited resolution have been reproduced by this theory in a number of non hydrogenic systems.[15,16] However, discrepancies between theory and experiment have been discovered in investigations of interference-narrowed Na and Rb Stark resonances. In some cases in sodium,[18] lifetimes were measured to be up to 20% shorter than the value predicted by WKB-QD theory; more recently Yang *et al.*[19] have reported some inconsistencies in electric field calibrations based on narrowings in Rb. These discrepancies are attributed to the semiclassical approximations used in the theory. These measurements on the alkalis as well as the work by van de Water *et al.*[6] on the triplet states of He provide the motivation to conduct further stringent tests of the WKB-QD theory.

We have made a systematic study at high resolution of the Stark structure of selected Rydberg states of helium. We extend the previous work[3,6,18,20] by making a quantitative study of the line shapes, concentrating on regions away from anticrossings where the resonances are well described by Fano profiles.[9,10] It is particularly convenient to work with the ^{4}He atom since in the singlet series fine and hyperfine structure is absent, the quantum defects are small and accurately known, and the "spaghetti" region where numerous narrow resonances experience strongly avoided crossings is smaller than in

any other atom. This allows us to track levels associated with hydrogen Stark quantum numbers and measure energies, widths, and asymmetry parameters over a wide range of field values. In this relatively simple case, any discrepancies that appear between theory and experiment should be easier to access and yet are not necessarily smaller in this system than a more complicated one. At the same time, the widths of the Stark resonances of helium are much narrower than in other atoms (for the same field and energy), and a direct measurement of the photoionization cross sections requires high-resolution laser techniques. Precise measurements of Stark resonance line shapes have been attempted in a few of the experiments mentioned above[9,10] but they have often been limited by signal to noise problems and inadequate energy resolution. Our techniques enable us to measure linewidths and asymmetries, both of which are accurate in the best cases to within 6%. These are among the most precise measurements so far made of line-shape parameters in the Stark effect.

In this investigation we characterize the evolution of the diabatic states of greatest slope arising from the zero field $n=32$ and $n=40$ manifolds. They can be labeled by the parabolic quantum numbers $(n,n_1,n_2,|m|)$, as (32,31,0,0), (32,0,31,0), and (40,0,39,0). We trace the evolution of the autoionizing line shapes from below the classical saddle-point energy, at which ionization first occurs, until the states disappear into the continuum. These states of extreme dipole moments were chosen to explore their contrasting ionization behavior. The principal quantum numbers of the states were selected for experimental convenience: their energies are low enough for the core-induced linewidth ($\propto n^{-4}$) to be considerably greater than the experimental resolution and for errors arising from field inhomogeneities and stray electric fields to be kept at a reasonable level. Yet they are high enough in energy to make it convenient to follow their entire evolution using a modest range of electric fields, determined by the saddle-point and parabolic critical thresholds (defined below). For isolated states in the region above the saddle point, WKB-QD theory predicts that the resonances will appear as Fano profiles. We compare experimental and theoretical widths, relative energies, and asymmetries by fitting both the experimental and theoretical line shapes to Fano profiles.

II. THEORY

The ionization of a Stark resonance state in a nonhydrogenic atom separates into two regions corresponding to two different decay processes. The first region starts just above E_{sp}, the classical saddle-point energy (in a.u.),

$$E_{sp}=-2\sqrt{F} \tag{1}$$

where $E=0$ corresponds to the zero-field ionization energy and F is the electric field. For sufficiently small energies above E_{sp}, the decay occurs primarily through a process, similar to autoionization,[21] in which hydrogenic basis states are coupled by the core perturbation to degenerate continuua. This coupling is absent for the nonrelativistic hydrogen atom because of the dynamical symmetry of the Coulomb-Stark potential. The ionization rate of a particular resonance in this region generally varies slowly with field and energy, except for local regions near crossings where the rates may either increase or decrease (often by orders of magnitude), depending on which particular states are coupled at the anticrossing. In the second region, at higher fields, the electron escapes by tunneling through the barrier appearing in the Stark potential. This behavior occurs when the resonance energy approaches the "parabolic critical threshold," given by

$$E_c=-2(\beta_2 F)^{1/2}\ , \tag{2}$$

which describes the top of the barrier in the effective potential for hydrogen,

$$V(\eta)=-\frac{\beta_2}{\eta}+\frac{|m|^2}{8\eta^2}-\tfrac{1}{4}F\eta\ , \tag{3}$$

along the parabolic coordinate η. (See Fig. 1.) In this tunneling region, where the atom will ionize even in the absence of core interactions, the resonances will broaden exponentially with field, until they join the continuum. The extent of the core-induced ionization region, the first region, is therefore determined by the separation constant β_2, which is the effective nuclear charge governing the motion along the coordinate η. The separation parameter $\beta_1=1-\beta_2$ similarly determines the motion along ξ, in which

$$V(\xi)=-\frac{\beta_1}{\xi}+\frac{|m|^2}{8\eta^2}+\tfrac{1}{4}F\eta\ . \tag{4}$$

β_2 varies from slightly less than 1 for the most red-shifted "anodic" state to slightly greater than zero for the blue-shifted "cathodic" state.

For a given n manifold, the effective potential barrier

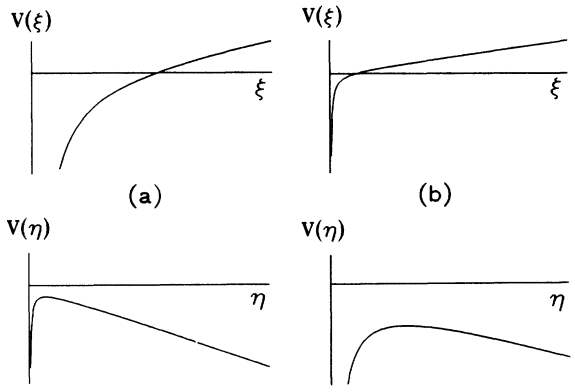

FIG. 1. Schematic plots of the potentials $V(\xi)$ and $V(\eta)$ for the hydrogen Stark effect for the two extreme sloping states in the Stark manifold. (a) The most blue-shifted state, with separation constant β_2 close to zero, where the electron is confined to small values of η, with $r\simeq z$, (i.e., along the electric field direction). (b) The most red-shifted state, with separation constant β_2 close to 1, where the electron is confined to small ξ, with $r\simeq -z$ (i.e., opposite to the electric field direction). The parabolic critical threshold occurs at the maximum value of the potential $V(\eta)$.

presented by Eq. (3) is least for the most red-shifted (small n_1, large β_2) and greatest for the most blue-shifted levels. Hence among Stark levels associated with a given n manifold in hydrogen, stability *increases* as one goes to progressively more upward-going levels. The helium core introduces only a slight coupling between quasidiscrete hydrogen Stark states, so the energy shifts in helium relative to hydrogen are small. However, small core-induced couplings between quasidiscrete Stark states and degenerate hydrogen Stark continua are often sufficient to produce ionization rates very much larger than the tunneling rates for the corresponding hydrogen states. The contrasting behavior of widths of the extremal states of a given hydrogen n manifold can thus be observed directly in helium only at fields sufficiently large that hydrogen-like tunneling predominates over core-induced ionization.

The WKB-QD theory has been described in the literature and only the results relevant to the present experiment are summarized below. The cross section for single-photon excitation with π-polarized light of energy $\hbar\omega$, from the metastable $2\,^1S$ state to the He Stark continuum is given by the following expression:[16]

$$\sigma^F(E)=4\pi^2\alpha\hbar\omega|\langle 2\,^1S|Z|\Psi_{E10}\rangle|^2 D^F(E) \tag{5}$$

in which Ψ_{E10} is the p component of the final state wave function with energy E and $m=0$. The field-independent dipole strength $|\langle 2\,^1S|Z|\Psi_{E10}\rangle|^2$ factors out from the Stark resonance structure contained in $D^F(E)$, the nonhydrogenic density of states. To evaluate Eq. (5), the required zero-field $s\rightarrow p$ matrix elements are calculated in the phase-shifted Coulomb approximation, integrating Schrödinger's equation in from a large radius at an energy corresponding to the effective principal quantum number. $D^F(E)$, which depends on the atom's quantum defects and hydrogen Stark parameters, is calculated using the WKB method in parabolic coordinates.[16] Quantum defects for He are obtained with high precision from Martin's recent work.[22]

It is shown in Ref. 16 that Eq. (5) reduces to the form of a Fano profile plus a background term in the limit in which a resonance is isolated:

$$\sigma^F(E)=C+\frac{D(q+\varepsilon)^2}{1+\varepsilon^2}\ , \tag{6}$$

where

$$\varepsilon=\frac{E-F_0}{\frac{1}{2}\Gamma}$$

measures the energy with respect to the line center E_0, in units of its half-width $\frac{1}{2}\Gamma$, q is the asymmetry parameter, and C and D are constants. For the case in which the atom has a single, non-negligible, and relatively small quantum defect δ_l, (as is approximately true for the Rydberg states of singlet He) these parameters can be expressed very simply in terms of δ_l and quantities that derive solely from the hydrogen-Stark structure:[16,23]

$$E_0\simeq E_H-\alpha\sin\delta_l\ , \tag{7a}$$

$$\Gamma\simeq\Gamma_H+2B\alpha\tan^2\delta_l\ , \tag{7b}$$

$$q\simeq-\cot\frac{\delta_l}{B}\ . \tag{7c}$$

E_H and Γ_H are the center and full width of the hydrogen-Stark resonance, B is the hydrogenic continuum background, and α is the resonance amplitude in the hydrogenic cross section $\sigma_H^F(E)$ for an isolated state:

$$\sigma_H^F(E)\simeq B+\alpha\frac{\frac{1}{4}\Gamma_H}{(E-E_H)^2+(\frac{1}{2}\Gamma_H)^2}\ . \tag{8}$$

Approximate analytic expressions for the hydrogenic background B have been derived in Ref. 24. For the conditions of the present experiment, in which pure $m=0$ states are excited in a one-photon transition, it takes the form

$$B\simeq 1-x\ , \tag{9}$$

where

$$x=\left[\frac{E}{E_{sp}}\right]^2\ .$$

The hydrogenic amplitude α is related to the transformation between spherical and parabolic coordinates and the energy spacing between the resonances.[6] As the electric field tends to zero, α is simply proportional to a Clebsch-Gordan coefficient:

$$\alpha^{F=0}=\frac{1}{\pi n^3}|\langle lm|j\mu_+j\mu_-\rangle|^2\ , \tag{10}$$

where $j=(n-1)/2$, $\mu_\pm=(m\pm nA_z)/2$, and $A_z=1-2\beta_2$ is the z component of the Runge-Lenz vector. Since the s quantum defect (0.139) for He is more than ten times larger than all other quantum defects, Eqs. (7a)–(7c) give reasonable estimates of the variations of the resonance parameters for a given channel. Excellent fits to Fano profiles for both the theoretical [Eq. (5)] and experimental line shapes are obtained for the field-energy regions studied in this work, as will be shown below.

Although the Stark resonances of helium show large deviations in their ionization behavior from those of hydrogen, and pronounced asymmetry in their profiles, their energies never stray more than about 0.06 cm^{-1} from hydrogenic values in the region of interest, because of the small magnitude of the He quantum defects. This justifies our labeling the helium states by hydrogen parabolic quantum numbers. Furthermore fourth-order perturbation theory for hydrogen[12] is often sufficient to make reliable spectral identifications in helium.

To construct accurate Stark maps in the low-field region below the classical saddle point, it is convenient to use the method described by Zimmerman *et al.*,[1] which employs matrix diagonalization in a truncated spherical basis. An analytical formulation of the WKB-QD theory[17] is also applicable in this region, but we have used the former method because it is somewhat easier to employ. In the high-field regime where the Stark and Coulomb potentials are comparable, the required number of spherical basis states in the matrix becomes exceedingly large and a different technique is necessary. Actually, for $n>30$, the spherical basis approach becomes cumbersome at fields not far beyond the first $\Delta n=1$ crossing. One possibility is to numerically search for and fit reso-

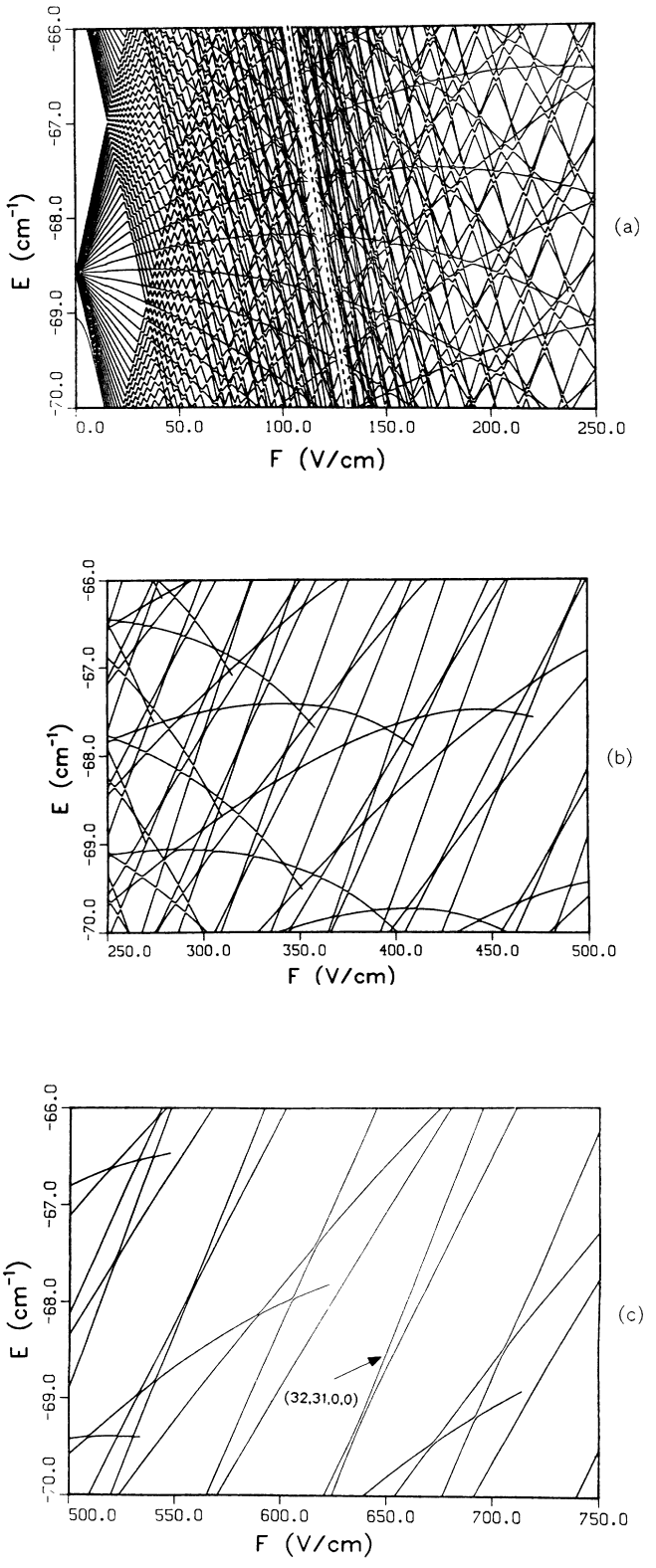

FIG. 2. Calculated Stark map using diagonalization in spherical and parabolic bases for low (0–15 V/cm) and high fields (15–750 V/cm), respectively. At zero field, the entire $n=40$ manifold is nearly degenerate near -68.6 cm^{-1}, except for the $69s$ state just below -69 cm^{-1}. The classical saddle-point threshold is shown by the dotted line in (a). The levels are terminated at their parabolic critical thresholds.

nances in $\sigma^F(E)$ [Eq. (5)] at successive values of energy and field. Because this is somewhat time consuming for studying broad spectral regions, we have used an alternative approach based on the multicontinuum autoionization model developed in Ref. 23. This technique allows one to follow the evolution of a given resonance with field by simultaneously tracking its energy, width, asymmetry, and intensity through various crossing regions. The model relates these resonance parameters to quantities easily calculated with the WKB-QD theory. For example, the Stark energies and widths are eigenvalues of a complex symmetric Hamiltonian, whose matrix elements are computed using the WKB-QD method. Figure 2 shows a calculation of the resonance energies for a broad region that includes the $n=40$ manifold at low fields and the (32,31,0,0) state at higher electric fields. The Zimmerman method has been used up to 15 V/cm, close to the first avoided crossings between $n=40$ and 41. For higher fields, the energies are calculated using the autoionization model. Complex symmetric matrices as described in Ref. 23 are diagonalized at intervals of 0.2 V/cm over segments of 20–50 V/cm. The basis includes all parabolic states that intersect the energy interval -70.5 to -65.5 cm^{-1} over these field segments. As many as 110 and, at the high-field end, as few as 20 basis states are needed. Off-diagonal elements account for interference effects analogous to those reported previously in Refs. 3, 5, and 18. For the isolated states studied in the present work, the diagonal terms dominate, and by themselves furnish useful predictions of the He Stark structure, as will be shown later. The levels in Fig. 2 terminate whenever the resonances pass above their parabolic critical threshold and join the continuum. The surviving resonance structure at high fields consists mainly of relatively isolated upward-trending states. Maps such as Fig. 2 have been useful in locating Stark resonances in helium.

III. EXPERIMENTAL METHOD

A. The experimental arrangement

The main elements of the experimental arrangement are shown in Fig. 3. The incident He($2\,^1S$) metastable beam is generated in a discharge in a pulsed supersonic expansion that has been described previously.[25] The discharge creates metastables, ions, electrons, and uv light. Most of the uv light is blocked by baffles. The charged species are deflected to remove them from the atomic beam, which is then collimated by a 1-mm skimmer 14 cm from the source. Since it is difficult to initiate a discharge in pure helium, we have found that a mixture containing 10% H_2 improves the shot-to-shot stability and enhances the metastable flux. Other additives, such as N_2, Ar, and Ne were found to quench the metastable beam.

The Rydberg states are excited using a high-resolution pulsed laser system, consisting of a single mode cw ring dye laser whose output is amplified in a three-stage excimer pumped amplifier chain. The output of the amplifier is frequency doubled into 10-ns uv pulses near 313 nm,

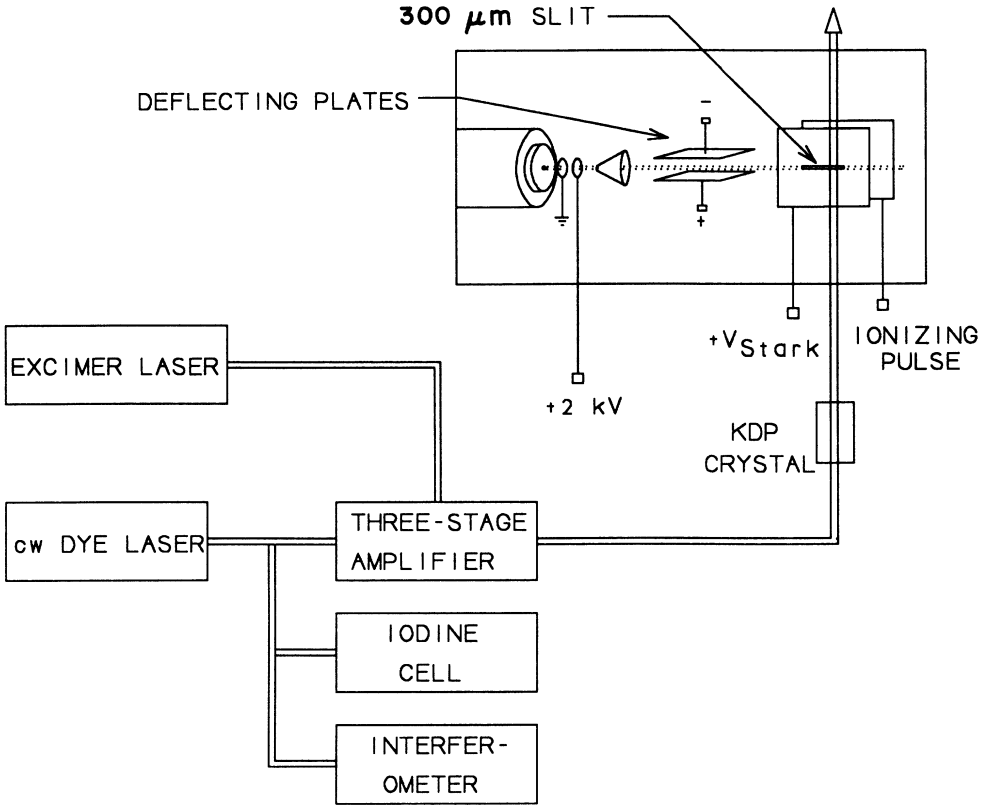

FIG. 3. Apparatus used for precise Stark spectroscopy of metastable helium.

having an energy of about 200 μJ and a nearly transform-limited bandwidth. In the remainder of the paper, all references to frequency differences refer to this frequency-doubled beam, not to the fundamental. The pulse energy is sufficient to saturate the transitions for most of the levels studied and thus neutral density filters are generally used to decrease the laser intensity. The data runs are taken with the laser scanned at 66 MHz/s, so that a broad 2–4 cm^{-1} scan lasts 15–30 min. Relative energies are determined to about 30 MHz accuracy by linearizing laser scans using fringes from an interferometer with a free spectral range of 597.54 MHz. Absolute line positions are determined to about 0.03 cm^{-1} using a wavemeter on the cw laser and monitoring the absorption spectrum of iodine vapor.

The unfocused laser beam enters the interaction region between two parallel plates at right angles to the atomic beam. The polarization of the light is adjusted to be along the z axis, normal to the capacitor plates. Only states with azimuthal quantum number $m=0$ are excited in this one-photon transition since the initial state is $2\,^1S$.

The pure linear polarization of the laser beam is verified in Fig. 4(a), an experimental scan over the $n=40$ manifold at $F=11.8$ V/cm. It reproduces rather closely the calculations shown in 4(b) for $m=0$ in which the low-field matrix diagonalization approach of Zimmerman *et al.*[1] has been used, with a limited basis set of 162 spherical states. In particular, the $m=0$ spectrum goes through a minimum near the middle, where any transitions to $|m|=1$ would still have large intensities, as seen in Fig. 4(c). This minimum for the $m=0$ components occurs because states in the middle of the manifold have wave functions distributed symmetrically along the z axis and thus the transition moment from the initial $2\,^1S$ state is zero. On the other hand, states near the extreme red

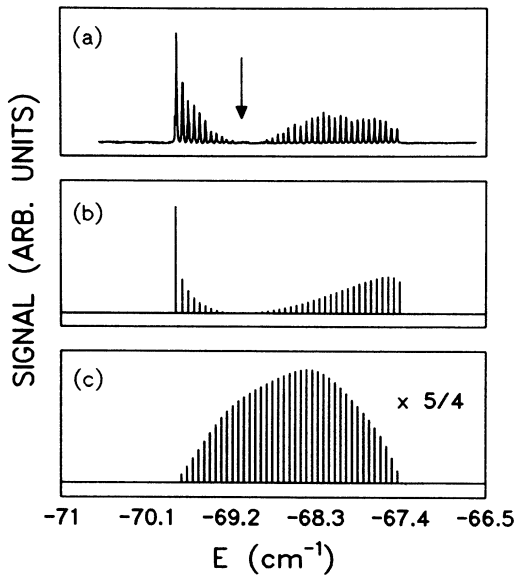

FIG. 4. (a) Experimental scan over the $n=40$ manifold at 11.8 V/cm. Theoretical spectra at the same field for the components with $m=0$ (b) and $|m|=1$ (c) demonstrate that the laser excitation in our experiment was to pure $m=0$ states. Theoretical intensities are obtained by diagonalization in a basis of 162 spherical states.

and blue edges have induced dipole moments along the z axis and thus carry most of the oscillator strength. This is true even at high fields: the steeply sloping states are always the strongest features in our $m=0$ spectra, while states with small slopes tend to be much weaker and also more asymmetric.

Since the states of extreme dipole moment studied here are the most steeply sloping with electric field, their experimental line shapes, especially their widths, are unfortunately the most sensitive to field inhomogeneities. The principal inhomogeneities in this experiment are spatial variations in the field across the diameter of the laser beam caused by deviations from parallelism of the field plates, and field perturbations associated with the grid or aperture in the upper plate through which electrons are collected. Studies of Stark plates by Metcalf and coworkers have shown that a thin slot on the collector electrode produces a more uniform electric field in the interaction region than even a carefully mounted grid.[18,19] A 0.30×25.4 mm^2 slot, electron discharge machined into the top plate, is used to collect photoelectrons produced by ionization. Both field plates are made from 0.25-in. brass, ground flat to less than 0.0001 in., and held apart by 1.0361-cm-long alumina spacers. In this way, an electric field uniformity of better than 1 part in 10^4 has been achieved across the interaction region. This results in an acceptably small broadening of the linewidths. The slot in the upper plate serves further to effectively collimate the atomic beam, since its long axis is positioned parallel to the atomic beam and perpendicular to the laser. This reduces the Doppler width to 10 MHz, negligible compared with the 100-MHz laser linewidth. The voltage across the plates is provided by a stable dc power supply, whose output is measured with a $5\frac{1}{2}$ digit voltmeter. To measure voltages exceeding 1 kV, a voltage divider was constructed from 1% resistors.

States that are stable (lifetimes >50 ns) in the electric field are detected by delayed Stark ionization with a large pulsed field, while autoionizing resonances are detected using the dc field to collect the resulting electrons. The signal from the electron multiplier is processed by a gated integrator and is subsequently acquired by a microcomputer.

B. Field calibration

In this work, the accuracy with which the electric field must be calibrated is determined from the behavior near the two critical field values. At the saddle-point and tunneling thresholds, the widths vary most rapidly with field, typically by 1% for changes of 1 part in 10^3 in the electric field. Thus a very simple calibration obtained by measuring the plate spacings and the applied voltage to 0.1% is sufficient, since other constraints limit the obtainable linewidth accuracy to 6–20 %.

It is interesting to compare this calibration with that obtained by matching experimental and theoretical spectra. We did this in two different ways. In the first method, we used the field mapping techniques suggested in Refs. 18 and 19. Here one takes advantage of resonances whose lifetimes increase dramatically over an extremely small increment in electric field. The maximum lifetime occurs at a unique electric field and energy. These local lifetime stabilizations occur because of destructive interference effects in the decay of the states mixed by the electric field. Figure 5 demonstrates this effect in He. We tuned to the peaks in energy of seven fairly pronounced narrowing regions in He (listed in Table I), and recorded the voltage applied to the plates that produced the largest signals with a detector arranged to detect only long-lived states. The maximum in the signal then corresponds to the minimum in the state's decay rate. By comparing these voltages with the theoretically predicted electric fields for each field-induced narrowing, we were able to obtain several independent values for the plate spacing. The average value so obtained was 1.0353(3) cm. By examining different narrowings separated by large voltages we also verified that the field was linear with voltage. These narrowings are easily located, and their reproducibility was checked daily to ascertain that the field calibration did not drift due to instrumental problems or surface charging effects. This method produced no surprises in that the calculated plate separation was consistent with direct measurements of the plate spacing, 1.036(1) cm. By explicitly measuring the field dependences of the lifetimes of the narrowed Stark components, one can obtain a much more precise electric field calibration, an application that has been explored in Refs. 18 and 19 for the case of Na and Rb Stark structure.

We also checked our absolute field calibration by measuring relative energies between several sharp lines located close to the saddle-point limit. Figure 6 shows the experimental and theoretical spectra in a region that includes the prominent (32,31,0,0) state. The theoretical electric field value shown in the calculated spectrum, 253.57 V/cm, was chosen to be that which produced the smallest rms deviation (32.4 MHz) with experiment.

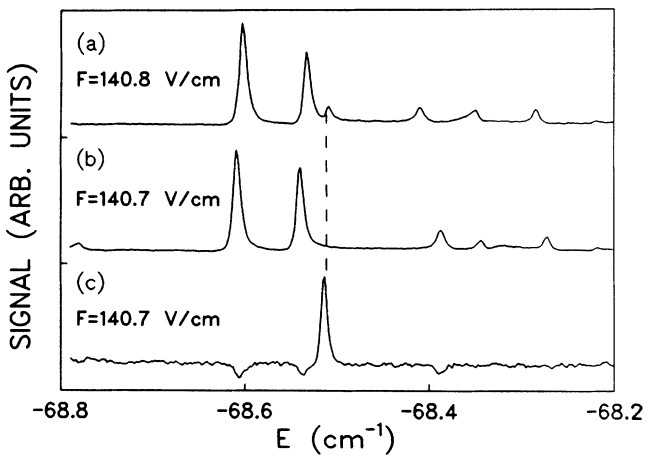

FIG. 5. Field-induced narrowing in He. As the electric field is tuned through the anticrossing from (a) 140.8 V/cm to (b) 140.7 V/cm, one of the resonances near -66.5 cm^{-1} disappears from the 50-ns window used for observing prompt autoionizing resonances. The resonance lifetime has suddenly increased to >1 μs and can be detected by applying a small delayed electric field pulse to ionize the atom, as shown in (c).

TABLE I. Calculated energies, maximum lifetimes, and relative intensities of interference-narrowed resonances in helium. The maximum lifetimes and intensities occur close to anticrossings. Away from these locations, the lifetimes and intensities decrease rapidly with energy and field.

Field (V/cm)	Energy (cm^{-1})	Maximum lifetime (nsec)	Relative intensity
359.00	−85.226	149	0.21
362.284	−86.552	132	0.27
365.15	−84.863	118	0.23
361.35	−85.211	689	0.054
358.004	−86.889	433	0.16
370.596	−84.466	1307	0.047
718.7	−64.68	424	0.03

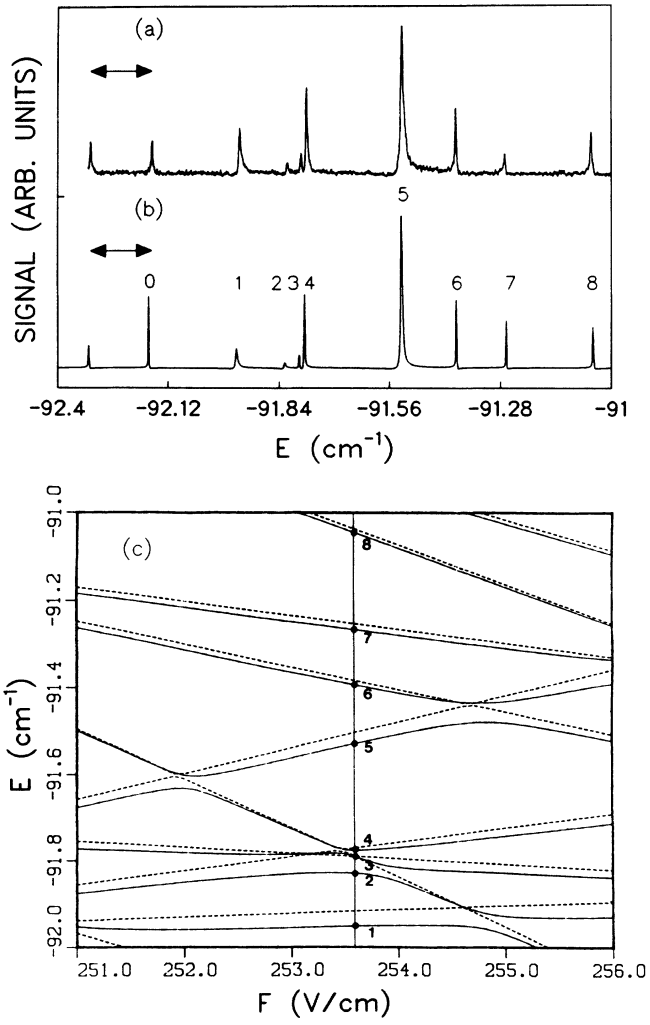

FIG. 6. (a) High-resolution scan showing relative energies of several resonances. (b) Theoretical spectrum calculated for 253.57 V/cm, slightly above the classical saddle-point threshold for $n=32$. The intrinsic linewidths in this region are narrower than the experimental resolution, so the experimental resonances appear somewhat broader and less intense than in the theory. (c) Stark maps of this region for He (solid line) and for hydrogen with nuclear mass 4 (dashed line), calculated using the autoionizing model described in the text.

Since the spacing between lines with highly disparate slopes changes very rapidly with electric field, these measurements are extremely sensitive to the absolute electric field value. The experimental uncertainty of 29 MHz for the strongest peaks, labeled "5" and "6" in Fig. 6, corresponds to a change of about 0.01 V/cm, implying a sensitivity of greater than 50 ppm to the electric field value. The match of the best-fit theoretical spectrum (Table II) is excellent, with most deviations less than half the laser bandwidth. Experimentally determined relative line positions deviated by less than 50 MHz from day to day for all except the smallest and therefore noisiest features. The voltage applied to the plates for this particular scan, 262.52(1) V, corresponds to a plate spacing of 1.035 30(4) cm, again consistent with the determinations mentioned above.

C. Field inhomogeneity

As discussed in Sec. III A, electric field inhomogeneities limit the accuracy of the measured line-shape parameters. The inhomogeneity was studied using several methods to monitor changes in the electric field as the laser beam was translated independently in the vertical and longitudinal directions. The most direct method is to tune the laser to the center of a narrow resonance, then to precisely measure the voltage change needed to regain the original signal intensity after the laser beam is translated. This was done by tuning both to very steeply sloping states [such as (32,31,0,0)] and to the sharp interference-narrowed Stark resonances described in Sec. III B. Another inhomogeneity measurement was performed by scanning the laser frequency, using an interferometer to monitor the relative shifts in the resonance positions as the laser beam position was moved between one scan and the next. Finally, observations of linewidths greater than the laser bandwidth in scans taken below the classical ionization threshold were used to place limits on the field inhomogeneity. The measurements taken by translating the laser beam indicated that the electric field in the longitudinal direction was nonuniform by 3.4 parts in 10^5 per millimeter and that the electric field in the vertical direction was nonuniform by 5 parts in 10^5 per millimeter at the center of the plates. The vertical electric field was found to decrease as one moved towards the slot, in agreement with calculations for an ideal slot.[19] The longitudinal electric field was found to vary linearly across the laser beam, consistent with a slight tilting of the plates due to small variations (0.0012 in.) in the plate spacing that could easily arise from nonuniform compression against the spacers.

IV. DATA ANALYSIS

The raw data are slightly distorted due to several experimental factors, including Doppler broadening, laser bandwidth, field inhomogeneities, and depletion broadening. Each of these effects was measured so that corrections could be applied to the data and the associated uncertainties could be estimated. These corrections are fairly small (ranging from 0–20 % of the linewidth) for all of the data points except those few taken just above the clas-

TABLE II. Separations between adjacent lines in 40 GHz continuous scans over the region shown in Fig. 6. The first column identifies the pairs of lines labeled in Fig. 6. The second and third columns gives the average experimental relative interval and the difference between the theoretical and experimental interval, respectively. The estimated experimental uncertainty is determined mainly from run-to-run scatter. The last column gives the relative slope between the adjacent lines. The average deviation between experimental and calculated intervals, weighted by the experimental uncertainties, is 32.4 MHz. Values in parentheses denote uncertainties.

Interval	Experiment (MHz)	Theory-Experiment (MHz)	Relative slope ($cm^{-1}/V/cm$)
0–1	6690(26)	−36	−0.078
1–2	3680(47)	−41	−0.015
2–3	1032(57)	81	0.066
3–4	402(27)	−27	0.076
4–5	7426(20)	−7	−0.052
5–6	4124(29)	28	−0.100
6–7	3774(33)	9	0.020
7–8	6616(30)	8	0.056

sical threshold, and simple first-order models are sufficiently accurate for the analysis. Figure 7 shows a typical uncorrected experimental spectrum and the corresponding theoretical spectrum near 440.7 V/cm. It is clear from the residuals that experimental line shapes are only slightly affected by the instrumental resolution. This figure also demonstrates that the resonance parameters—widths, asymmetries, energies, and intensities, are well defined and may be used to compare experiment with theory.

The data reduction procedure we followed was somewhat different for the $n=32$ and 40 measurements, since the $n=32$ data spanned a much wider range of electric fields. The procedure followed for $n=32$ consists of several steps.

(i) Estimate the broadening due to the electric field inhomogeneities discussed in Sec. III C by measuring the laser spot size and using the known Stark slope to determine the contribution to the linewidth at each field value.

(ii) Determine the line-width arising from laser and Dopper broadening by measuring narrow resonances below the ionization threshold.

(iii) Study the saturation of the transitions as a function of laser power to determine the effects of depletion broadening. Use a simple model to remove saturation effects from the experimental data.

(iv) Combine the widths due to laser linewidth, Doppler broadening, and inhomogeneity across the laser beam to determine an effective instrument function for each field value.

(v) Explicitly deconvolute this instrument function from the data using fast Fourier transforms, to obtain the "corrected" spectrum. A least-squares fit to Fano line shapes is then performed.

In the following sections these steps are discussed in more detail. The treatment of the $n=40$ data is discussed separately in the last section. Table III lists the corrections and uncertainties applied at each stage of this data reduction process, for five typical runs taken at various electric fields strengths.

A. Field inhomogeneities

Errors due to field inhomogeneity arose predominantly from the longitudinal atomic beam spread over the small region of the laser spot, whose dimensions were 1.50(75) mm [full width at half maximum (FWHM)] in the longitudinal (y) direction and 0.6(3) mm (FWHM) in the vertical (z) direction for most of the measurements. The electric field in the y direction varies approximately linearly across the atomic beam over a range, $\Delta F(y)$, given by the product of the fractional inhomogeneity, 3.4×10^{-5} per mm, the distance y from the center of the laser spot, and the electric field F. The corresponding frequency spread $\Delta\omega(y)$ is then determined by the slope of the Stark resonance: $\Delta\omega(y)=\mathcal{S}\Delta F(y)$, where $\mathcal{S}$ is the slope. The calculated values for $\Delta\omega$ across the full width of the laser spot range from 23.0(11.5) MHz at 251 V/cm to 126(63) MHz

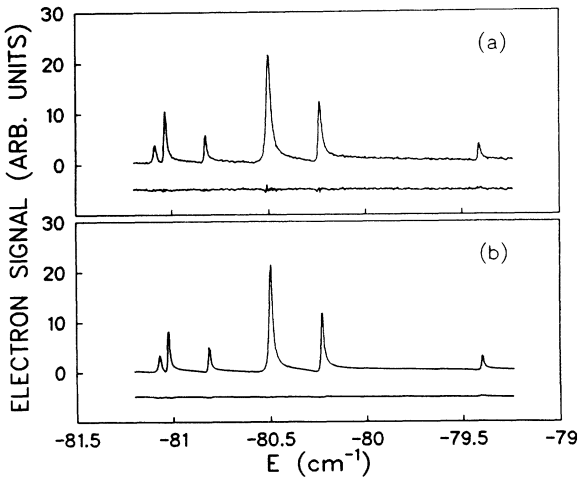

FIG. 7. (a) Uncorrected experimental spectra and (b) theoretical spectra at 440.7 V/cm. The residuals from fits to six Fano profiles are given below the scans. The absolute intensity of the experimental spectrum has been normalized at a single point to correspond to the theoretical intensity at that point.

TABLE III. Typical values for the corrected widths, q values, and the estimated uncertainties accumulated at each of the three stages in the data reduction process described in the text. "Raw," "desat," and "deconv" refer to parameters obtained from fitting Fano profiles to the raw, desaturated, and deconvoluted data, respectively.

State	(32,31,0,0)	(32,31,0,0)	(32,31,0,0)	(40,0,39,0)	(32,0,31,0)
Field (V/cm)	251	570.1	1498.5	251	607.8
f [Eq. (14b)]	0.18	0.213	0	0	0
Γ_{raw} (MHz)	173(9)	900(34)	2040(193)	340(17)	565(37)
Γ_{desat} (MHz)	166(10)	850(41)	2040(193)	340(17)	565(37)
Γ_{deconv} (MHz)	97(40)	816(48)	2014(209)	324(22)	500(56)
q_{raw}	11(2)	11.0(10)	6.7(43)	53(20)	32(25)
q_{desat}	11(2)	11.4(10)	6.7(43)	53(20)	32(25)
q_{deconv}	16(3)	11.6(12)	6.7(43)	75(35)	39(25)

at 1498 V/cm for the (32,31,0,0) Stark component. The widths due to inhomogeneity were added in quadrature to the two widths in the scans taken below threshold described in Sec. IV B to obtain the effective instrument function. The uncertainty in the inhomogeneity arises primarily from the uncertainty in the laser spot size, which we measured to about 50% accuracy.

B. Laser and Doppler width

The combined effect of Doppler broadening and laser bandwidth is determined by fitting scans taken below the classical saddle point. Since the Doppler width is just 10 MHz, the line shape is determined almost entirely by the laser, with small contributions due to electric field inhomogeneity across the laser beam. A good fit to the measured line shapes can be obtained with a sum of two Gaussians. The broader Gaussian is centered 80 MHz to the blue of the narrow one and is a factor of 5 smaller. The origin of this unusual line shape is not known but it appears to be largely independent of discharge conditions, laser power, and electric field. The broad shoulder may arise from scattering of the atomic beam by the skimmer plates or from diffracted light around the laser beam, resulting in two slightly different velocity groups in the interaction volume.

To remove the slight broadening due to field inhomogeneities, the associated linewidth is calculated as described in Sec. IV A, and subtracted in quadrature from each of the two Gaussians. The resulting full widths at half maximum are 104(10) and 240(50) MHz for the large and small components, respectively. This laser line shape contributes less than 10% to the widths for the majority of the data points, while larger corrections are necessary for the few points in which the instrumental resolution and the natural width are comparable.

C. Depletion broadening

A final source of distortion is depletion broadening, the saturation of signal amplitude with increasing laser intensity due to the depletion of the metastable population. The amount of depletion varies across the laser beam since atoms in different dc fields and laser intensities have different ionization probabilities. The total number of atoms in a volume $d^3\mathbf{r}$ that remain in the metastable state at the end of a laser pulse is given by

$$dN(\omega_0,\mathbf{r})=\frac{N_0}{V}d\mathbf{r}\exp\left[-\int_{-\infty}^{\infty}\sigma(\omega,\mathbf{r})g(\omega-\omega_0)f(y,z)\times\int_0^{\infty}I(t)dt\,d\omega\right], \quad (11)$$

where N_0 is the initial number of metastables in the interaction volume V, $\sigma(\omega,\mathbf{r})\simeq\sigma(\omega-\Delta\omega(y))$ is the frequency- and position-dependent cross section, $g(\omega-\omega_0)$ is the laser bandwidth function given in Sec. IV B, $f(y,z)$ describes the spatial distribution of the laser beam, and $I(t)$ is the temporal laser pulse shape. The signal originating from a group of atoms located at $\mathbf{r}$ therefore saturates exponentially with increasing intensity.[26] As long as the laser intensity and dc field variations are small across the laser beam the total signal size

$$S(\omega_0)=N_0\left[1-\int_{\mathbf{r}}dN\right] \quad (12)$$

will also approximately exhibit this exponential behavior. Only then may we treat saturation and inhomogeneity effects separately. In this case we have approximately

$$S(\omega_0)\simeq N_0\{1-\exp[-I_0\sigma(\omega_0)^*G(\omega_0)]\}, \quad (13)$$

where $\sigma(\omega_0)^*G(\omega_0)$ is the convolution of the cross section with the total instrument function including bandwidth and inhomogeneity contributions added in quadrature, and the integral over the temporal laser pulse shape is given by I_0. The accuracy of Eq. (13) was checked under our experimental conditions by taking simulated Fano profiles for $\sigma(\omega_0)$, integrating Eq. (11), and then using the data analysis procedure based on Eq. (13) (discussed below) to extract $\sigma(\omega_0)$. The model recovered the original Γ and q parameters to better than 2%, and was therefore judged to be satisfactory.

At each resonance, we studied the signal size at the peak, $S(\omega_p)$, as a function of laser intensity. A least-squares fit to Eq. (13) was used to extract the saturation parameters N_0 and $\sigma(\omega_p)^*G(\omega_p)$ that characterize the transition. These parameters could then be used to solve Eq. (13) for the "desaturated" signal at frequency ω_0:

$$\sigma(\omega_0)^*G(\omega_0)=\sigma(\omega_p)^*G(\omega_p)\frac{\ln\left[1-\dfrac{fS(\omega_0)}{S(\omega_p)}\right]}{\ln(1-f)}, \quad (14a)$$

where

$$f \equiv 1 - \exp[-I_0 \sigma(\omega_p) * G(\omega_p)] \tag{14b}$$

and

$$S(\omega_p) = N_0 f \ .$$

Here $S(\omega_0)$ and $S(\omega_p)$ are given in the same (arbitrary) units and f is the fraction of saturation at the resonance peak. Data runs were generally taken at a saturation fraction of less than 25%, which provided enough signal to noise to obtain excellent fits, without unacceptably depletion broadening the transition.

D. Deconvolution

Since the "desaturated" data are still a convolution of the instrument function and a Fano profile [Eq. 14(a)], we decided to deconvolute the data using fast Fourier transforms. In this procedure the transform of the desaturated signal is divided by the transform of the instrument function, then the inverse transform is taken to obtain the resulting spectrum. The transform of the instrument function, which is nearly Gaussian, quickly approaches zero and therefore amplifies the noise component present in the signal. It is therefore necessary to eliminate a portion of the transformed signal before proceeding. This is equivalent to a low-pass filtering of the original data, and can result in unphysical oscillations and spectral broadening if the spectra are cut off too early, while excessive noise results if they are cut off too late. An appropriate compromise can be reached by examining the power spectrum of the data, which falls steeply before rising again due to noise. The cutoffs were chosen based on the power spectrum, together with a knowledge of the approximate linewidths of the underlying data, to avoid any measurable distortion of the line shapes, while still eliminating the worst of the noise amplification. Figures 8(a) and 8(b) show the uncorrected signal $S(\omega)$ and the deconvoluted cross section $\sigma(\omega)$ for a scan taken at 520 V/cm. The best-fit parameters for the raw data are $\Gamma = 794(26)$ MHz and $q = 8.3(4)$. After desaturation and deconvolution these parameters are changed to 734(43) MHz and 8.8(6).

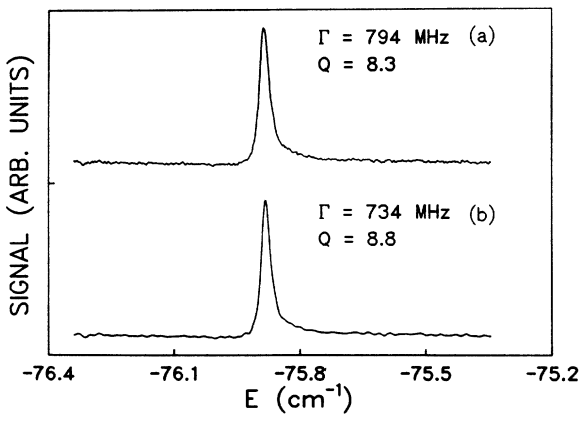

FIG. 8. (a) A typical raw data scan over the (32,31,0,0) resonance at 520 V/cm. After desaturation and deconvolution and with the instrument function the width decreased by 7.5% and the q parameter increased by 6%, as shown in (b).

Errors associated with the low-pass filtering in the deconvolution procedure were estimated for each run by reconvolving the deconvoluted line shape with the instrument function and comparing the resulting line-shape parameters with the original data. As an additional check, model Fano profiles with simulated random noise approximately equal to the experimental noise level were convoluted with the instrument function and then deconvoluted using the same cutoff criterion applied to the actual data. The resulting spectra were then compared with the original model Fano profiles, in order to estimate the deconvolution error. In both cases, the numerical procedure contributed errors usually much less than 5%, which were incorporated in the final error budget.

E. Error estimates

Typically, four to six runs are averaged for each value of the electric field. Statistical errors due to run-to-run scatter varied from 3% to 15% for the widths and from 5% to 40% for the asymmetry parameters. For each run, the errors in Γ and q due to the uncertainty in the measurements of laser bandwidth, field inhomogeneity, and laser power saturation are estimated by varying each of these independently by their uncertainties, and repeating the data reduction procedure using the new values. The total uncertainties are given by the rms sum of these systematic errors, the deconvolution error, and the statistical error. Because each data run has a different uncertainty associated with it, the mean values for Γ and q are determined by a weighted average. Measurements tend to be more accurate for data taken where the lines were neither very narrow (close to E_{sp}) nor very broad (close to E_c); near E_{sp}, the linewidths are comparable to the instrument function; close to E_c, the signal-to-noise ratio is relatively poor both because the background continuum strength is large and because the oscillator strength, which remains relatively constant for a given Stark component, is spread throughout the linewidth. Thus relatively larger statistical uncertainties occur in this region.

F. Analysis of $n = 40$ data

For the (40,0,39,0) level, the broadening due to a given inhomogeneity across the interaction region is larger than for $n = 32$ because the $n = 40$ level is almost three times more steeply sloping than (32,31,0,0) and approximately twice as steeply sloping as (32,0,31,0). In initial measurements of the (40,0,39,0) level, the linewidths observed below the ionization threshold suggested an inhomogeneity at least twice as large as any of the other determinations. The reason for this is not understood, although it may have resulted from accidentally displacing the laser beam vertically towards the slot in the upper electrode during the $n = 40$ measurements. In subsequent measurements of $n = 40$, we made two modifications that reduced the vertical and longitudinal inhomogeneity, respectively: The interaction region was displaced 1.3 mm below the center of the plates towards the solid electrode and a 1-mm aperture was placed in the laser beam path

to reduce the longitudinal spot size. These changes resulted in an inhomogeneity of 5(1) parts in 10^5 across the interaction region. This value was determined by comparing in scans below threshold the widths of levels with negligible Stark slope with the (40,0,39,0) width. The measurements based on translating the laser beam discussed in Sec. III C gave consistent results.

Because the (40,0,39,0) data were all taken at field values near the saddle-point threshold and at very low laser intensities, it was possible to combine steps 1, 3, and 4 mentioned above. The instrument function determined from scans taken just below threshold unavoidably includes the width due to inhomogeneities at the field value for which the calibration scan is taken. Since the onset of ionization is very rapid for this Stark component, the entire data set spans only a very limited range of fields from 245 to 252 V/cm, and the same inhomogeneity correction is applicable to all of the data. The data-taking procedure therefore consists of taking several scans below threshold, and then without changing the laser alignment measuring the line shapes above threshold. The (40,0,39,0) instrument function is then directly deconvoluted from the above-threshold data.

V. RESULTS AND DISCUSSION

Figures 9–13 show the main results of the present experiment: the energies, widths, and q values for the most upward going, and the widths for the most downward-going components in the $n=32$ and 40 manifolds at selected field values. It is seen in Fig. 9 that the energy for the upward-going state follows closely the corresponding (32,31,0,0) state in hydrogen, which is to be expected away from crossing regions. This was also true

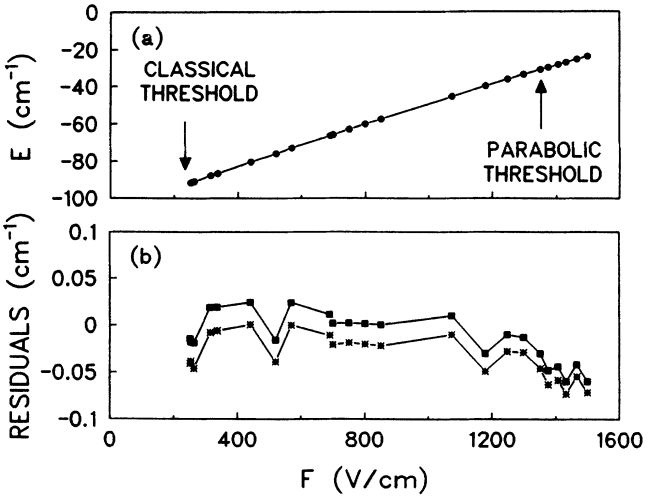

FIG. 9. (a) The energies of the (32,31,0,0) level away from avoided crossings, from the classical saddle-point threshold to the parabolic critical threshold. The behavior is very nearly hydrogenic. (b) The experimental energies subtracted from the WKB-QDT predictions (solid squares) and the experimental shifts relative to hydrogen with nuclear mass of 4 (asterisks). The residuals from the autoionization model are not plotted because they deviate by less than 0.001 cm^{-1} from the WKB-QDT results. Points are connected with a solid line for convenience.

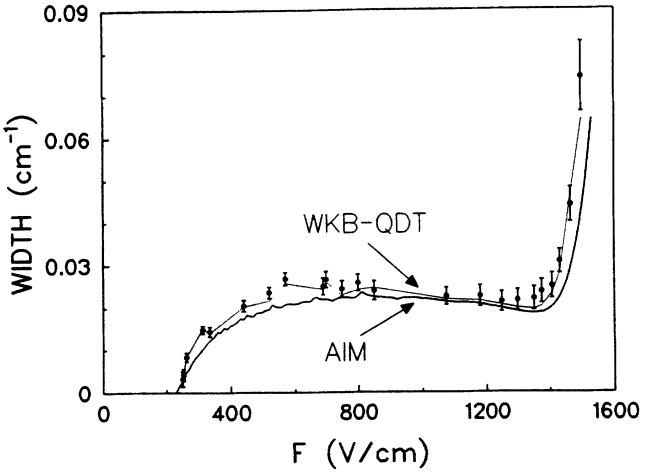

FIG. 10. Experimental and theoretical widths for (32,31,0,0). Solid circles give the experimental results, the dashed and solid lines are the WKB-QD and autoionization model (AIM) predictions, respectively, at the same field values as in the experiment. The theoretical results are connected with smooth lines for convenience.

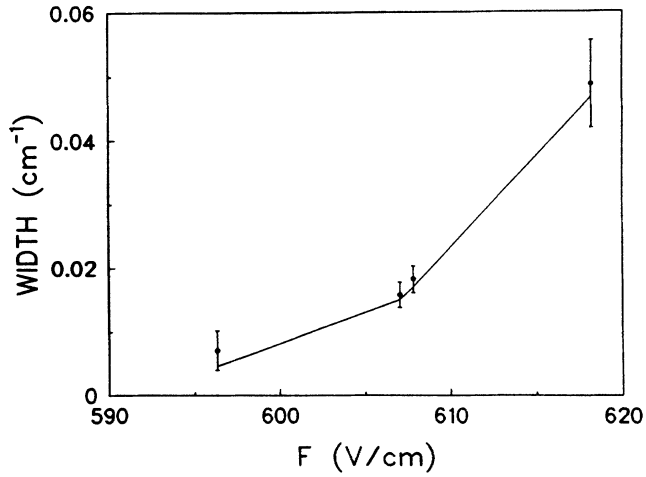

FIG. 11. Experimental and WKB-QDT widths for the (32,0,31,0) level, shown as in Fig. 10.

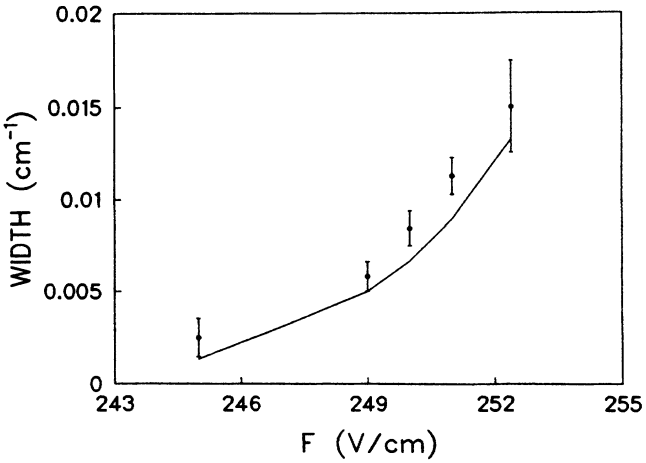

FIG. 12. Same as Fig. 11, but for the (40,0,39,0) level.

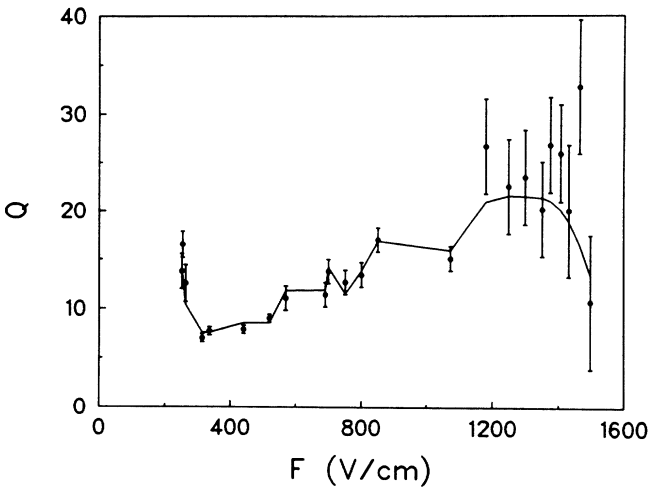

FIG. 13. Asymmetry parameters for (32,31,0,0) at the same field values as in Figs. 9 and 10. Experimental results are shown together with the predictions of the WKB-QD theory.

for the downward-going states. The "zeroth"-order formula [Eq. (7a)] predicts the energy shift due to the He^+ core to be 0.05 cm^{-1}, while the average shift from hydrogen was measured to be 0.03 cm^{-1}.

Unlike the energies, the ionization rates are affected dramatically by the core perturbation, as can be seen in Fig. 10. For the most upward-going state, the core-induced ionization provides the dominant decay mechanism for a huge region spanning the interval between 250 and 1400 V/cm in field and 80 cm^{-1} in energy. After the initial rise above the saddle point, the (32,31,0,0) width reaches a plateau where it remains relatively constant until the parabolic critical threshold where it sharply increases. Theoretically, there should even be a slight dip in the width before the final exponential rise, though the dip is not as pronounced in the experiment. As pointed out in Ref. 23, these general trends in the widths are also expected (and may even be more dramatic) for other Rydberg atoms. This can be discerned from the approximate expression for the core contribution to the width, $\frac{1}{2}\Gamma_c \simeq B\alpha \tan^2\delta_l$, in Eq. (7b). The hydrogenic continuum background B rises slowly from zero at the saddle-point energy to unity at the zero-field ionization limit, as more channels pass successively above their parabolic critical threshold. [See Eq. (9).] The resonance amplitude α, which depends on the relative amount of s wave contained in the Stark-shifted state, decreases in strength for increasing energies, due to dilution from mixing with states higher in energy. Although their product remains relatively constant, the resonance amplitude actually decreases faster than the continuum strength rises, accounting for a slight dip in the width. Taking B to be $\simeq 1$ (its high-field limit) and α to be its zero-field expression [Eq. (10)], the plateau width for He comes out to be 0.015 cm^{-1}, which is within a factor of 2 of the values (0.02–0.03 cm^{-1}) over the plateau region in Fig. 10. This level of agreement is typical of that found for this type of "zeroth"-order estimate for Stark resonances in sodium.[23]

Also plotted in Fig. 10 are the autoionization model's predictions for the widths for the (32,31,0,0) channel. Even though off-diagonal terms (crossing effects) have been excluded and a limited basis set has been used, there is good agreement between WKB-QD theory and this simplified theory. In particular, energies agree to better than 0.001 cm^{-1}, and ionization rates are slightly lower ($\simeq$20%) than predicted by WKB-QD theory. Because the autoionization model makes a distinction between discrete and continuum channels, discontinuities in the calculated line-shape parameters occur near the parabolic critical thresholds, as can be seen from small irregular jumps in Fig. 10. Whenever this occurs, the number of continuum (discrete) channels in the basis set increases (decreases) by one, resulting in a small loss in accuracy.[23]

The behavior of the width for the most downward-going "red" levels is dramatically different from the upward-going "blue" levels. For the red levels shown in Figs. 11 and 12, the saddle-point and the parabolic threshold are almost identical and thus there is little room for the core-induced width to play a significant role before exponential tunneling dominates the decay. The field dependence of the width looks very similar to hydrogen in this case.

The measured widths for $n=32$ are in most cases found to be slightly greater than the theoretically predicted widths, though they generally agree within the error bars. The widths near the parabolic critical threshold for (32,31,0,0) at 1350 V/cm are narrower (by up to 17%) in the theory than in the experiment, where the dip is not as prominent. On the other hand, the error bars are also somewhat larger in this region due to the significant statistical fluctuations that result from the large continuum background. The results for the corrected $n=40$ widths are shown in Fig. 12. Here the data are in reasonable agreement with the WKB-QD theory, with the largest discrepancies about two standard deviations in size.

One might have expected the WKB approximation used to calculate properties of hydrogen Stark wave functions to be somewhat inaccurate for the extremal Stark components. Even though the principal quantum numbers are large, the wave function for the most upward- and downward-going levels have a single node in the potentials $V(\eta)$ and $V(\xi)$, respectively, implying a small value for WKB wave number along these directions (see Fig. 1). Furthermore, at high fields, as the separation constant β_2 for the bluest channel approaches zero, the two classical turning points join together and there is no longer a distinction between the barrier and the well in the η potential.[14] It is somewhat surprising that isolated extreme Stark components, unlike interference-narrowed levels near anticrossings,[18,19] do not seem to show significant deviations from theory that can be attributed to failures in the WKB method.

Accurate measurements of the asymmetry parameter q are more difficult than for the widths because they rely on having a drift-free baseline with good signal to noise throughout the periphery of the line shape. Figure 13 shows the measured q values for the (32,31,0,0) level. Some of the uncertainties, especially for smaller q's, are less than 10%; in fact, this is perhaps one of the most accurate measurements of line-shape asymmetries that has

been made. The error bars become larger with increasing field since the signal size decreases. The fact that q increases at the same time makes it even more difficult to measure this parameter, since large but slightly differing q values are difficult to distinguish. Still, the general trend agrees remarkably well with the calculations. The late drop in q during the exponential rise in the width near 1350 V/cm occurs because the state becomes a shape resonance near the tunneling barrier, which causes a rise in the baseline on the high-energy side.[27–30] The q parameters for the downward-going (32,0,31,0) and (40,0,39,0) levels are very large for all isolated regions examined in the present experiment. This is due to the fact that the continuum background B is nearly zero close to the classical threshold field [see Eq. (7(c)].

VI. CONCLUSIONS

In this experiment, we have studied the energies, widths, and asymmetry parameters in helium for the extreme Stark components in the $n=32$ manifold and for the extreme downward-going component in the $n=40$ manifold. Because they are the most steeply sloping with field, these levels are the most sensitive to field inhomogeneities, which inevitably causes some distortion of the line shapes. The high resolution of the current experiment combined with the slot design for the electric field plates[18,19] minimizes this problem and makes it possible to determine accurate line-shape parameters for ionizing Stark resonances in helium. Our measurements have verified some interesting properties of the extreme Stark components.[31] (i) These states have the largest induced dipole moments, so that when excited with π-polarized light they tend to have larger cross sections than other states in the manifold. (ii) In isolated regions their energies follow very closely the corresponding hydrogenic energies. Properties (i) and (ii) make these levels extremely easy to identify in a spectrum. (iii) Yet, the ionization rates of the blue state differ dramatically from hydrogen while that for the red states is similar to hydrogen.

In regions away from level crossings, line-shape parameters have been shown to have a simple field dependence that is fairly accurately reproduced by an autoionization model. A similar field dependence has been predicted in Refs. 5 and 23 for sodium, but these are the first systematic experimental measurements of nonhydrogenic Stark line shapes over the full range of field values from E_{sp} to E_c. We have also compared relative energies, widths, and asymmetries with the more precise WKB-QD theory by fitting both theoretical and experimental line shapes to Fano profiles. The agreement between theory and experiment for relative energies is remarkable; if the theory is assumed correct, it implies that we have determined the absolute field value at the center of our plates to better than 50 ppm. This accuracy is substantially better than has so far been obtained using interference narrowings as a calibration,[19] since the narrowings are very sensitive to small changes in theoretical details that affect the mixing phase. However, precise energy-level measurements require narrowband lasers and are obviously more difficult to perform.

Confirmation of the theory for the widths and asymmetries of the extremal $n=32$ and 40 levels is obtained for all field and energy regions studied in this work, apart from small discrepancies for the $n=40$ linewidths. Because the signal to noise is worst in the tunneling regime, it would be useful to obtain more accurate measurements in this region, where the core modifies only slightly the line shapes from those of hydrogen.

ACKNOWLEDGMENTS

This research was supported by the National Science Foundation, Grant No. PHY-8717051.

*Present address: Department of Physics and Astronomy, University of Delaware, Newark, DE 19716.

[1]M. L. Zimmerman, M. G. Littman, M. M. Kash, and D. Kleppner, Phys. Rev. A **20**, 2251 (1979).
[2]P. M. Koch and D. R. Mariani, Phys. Rev. Lett. **46**, 1275 (1981).
[3]S. Feneuille, S. Liberman, E. Luc-Koenig, J. Pinard, and A. Taleb, J. Phys. B **15**, 1205 (1982).
[4]M. G. Littman, M. L. Zimmerman, and D. Kleppner, Phys. Rev. Lett. **37**, 486 (1976).
[5]J. Y. Liu, P. McNicholl, D. A. Harmin, J. Ivri, T. Bergeman, and H. J. Metcalf, Phys. Rev. Lett. **55**, 189 (1985).
[6]W. van de Water, D. R. Mariani, and P. M. Koch, Phys. Rev. A **30**, 2399 (1984).
[7]W. Davis, H. Metcalf, and W. Phillips, Phys. Rev. A **19**, 700 (1979).
[8]C. Chardonnet, D. Delande, and J. C. Gay, Phys. Rev. A **39**, 1066 (1989).
[9]S. Feneuille, S. Liberman, J. Pinard, and A. Taleb, Phys. Rev. Lett. **42**, 1404 (1979).
[10]T. S. Luk, L. DiMauro, T. Bergeman, and H. J. Metcalf, Phys. Rev. Lett. **47**, 83 (1981).
[11]R. J. Damburg and V. V. Kolosov, J. Phys. B **12**, 2637 (1979), and references therein.
[12]H. J. Silverstone, Phys. Rev. A **18**, 1853 (1978).
[13]E. Luc-Koenig and A. Bachelier, J. Phys. B **13**, 743 (1980); **13**, 1769 (1980); Phys. Rev. Lett. **43**, 921 (1979).
[14]D. A. Harmin, Phys. Rev. A **24**, 2491 (1981).
[15]D. A. Harmin, Phys. Rev. Lett. **49**, 128 (1982).
[16]D. A. Harmin, Phys. Rev. A **26**, 2656 (1982).
[17]D. A. Harmin, Phys. Rev. A **30**, 2413 (1984).
[18]P. McNicholl, T. Bergeman, and H. J. Metcalf, Phys. Rev. A **37**, 3302 (1988).
[19]D.-H. Yang, D. Lieberman, P. van der Straten, T. Bergeman, and H. Metcalf (unpublished).
[20]C. T. W. Lahaye and W. Hogervorst, Phys. Rev. A **39**, 5658 (1989).
[21]M. G. Littman, M. M. Kash, and D. Kleppner, Phys. Rev. Lett. **41**, 103 (1978).
[22]W. C. Martin, Phys. Rev. A **36**, 3575 (1987).
[23]P. McNicholl, J. Ivri, and T. Bergeman (unpublished).
[24]D. A. Harmin, in *Atomic Excitation and Recombination in External Fields*, edited by M. H. Nayfeh and C. W. Clark (Gordon and Breach, New York, 1985).
[25]E. E. Eyler, J. Gilligan, E. McCormack, A. Nussenzweig, and E. Pollack, Phys. Rev. A **36**, 3486 (1987).

[26]W. E. Cooke, S. A. Bhatti, and C. L. Cromer, Opt. Lett. **7**, 69 (1982).
[27]T. Bergeman, C. Harvey, K. B. Butterfield, H. C. Bryant, D. MacArthur, M. Davis, J. B. Donahue, J. Dayton, and W. W. Smith, Phys. Rev. Lett. **53**, 775 (1984).
[28]D. A. Harmin, Phys. Rev. A **31**, 2984 (1985).
[29]W. L. Glab and M. H. Nayfeh, Phys. Rev. A **31**, 530 (1985).
[30]G. Alvarez and H. J. Silverstone (unpublished).
[31]K. Ng, D. Yao, and M. H. Nayfeh, Phys. Rev. A **35**, 2508 (1987).